BNL-226346-2024-JAAM

GRP-COEE-39

Synergistic Anion and Solvent-Derived Interphases Enable Lithium-Ion Batteries under Extreme Conditions

S. Tan, E. Hu

To be published in "Journal of the American Chemical Society"

October 2024

Chemistry Department

Brookhaven National Laboratory

U.S. Department of Energy

USDOE Office of Energy Efficiency and Renewable Energy (EERE), Office of Sustainable Transportation. Vehicle Technologies Office (VTO)

DISCLAIMER

Synergistic anion and solvent derived interphases enable lithium-ion batteries under extreme conditions

Sha Tan[1], Oleg Borodin[2], Nan Wang[1], Dean Yen[1], Conan Weiland[3], Enyuan Hu[1*]

[1] Chemistry Division, Brookhaven National Laboratory, Upton, NY, USA 11973

[2] Battery Science Branch, Army Research Directorate, DEVCOM Army Research Laboratory, Adelphi, MA, 20783 USA

[3] Materials Measurement Science Division, Material Measurement Laboratory, National Institute of Standards and Technology, Gaithersburg, MD, 20899 USA

ABSTRACT: Lithium-ion batteries (LIBs) face increasingly stringent demands as their application expands into new areas, including extreme temperatures and fast charging. To meet these demands, electrolyte should enable fast lithium-ion transport and form stable interphases on electrodes simultaneously. In practice, however, improving one aspect often compromises another. For instance, the trend towards electrolytes forming anion-derived interphases typically reduces transport efficiency due to weak-solvating solvents. We propose that instead of relying on anions to form the interphase, leveraging both solvents and anions to form interphases can potentially lead to a balancing point between robust interphase formation and effective ion transport. Guided by this design principle, 2,2-difluoroethyl ethyl carbonate (DFDEC) has been identified as the promising solvent. With the new electrolyte using DFDEC as the major solvent and lithium bis(fluorosulfonyl) imide (LiFSI) as the salt, graphite||$LiNi_{0.8}Mn_{0.1}Co_{0.1}O_2$ full cells are capable of fast-charging and demonstrate long-term cycling stability with a cutoff voltage of 4.5 V. Notably, the battery shows the capacity retention of 84.3% after 500 cycles with an average coulombic efficiency (CE) as high as 99.93%. This new electrolyte also enables stable battery cycling across a wide temperature range (-20 °C to 60 °C), with excellent capacity retention and long cycle life.

INTRODUCTION

Lithium-ion batteries (LIBs) stand as the cornerstone of a clean energy society, playing increasingly pivotal roles, particularly in the electrification of transportation. The multifaceted application contexts of LIBs impose demanding requirements: they must operate efficiently at both low and high temperatures and possess fast charging capabilities. Addressing these demands necessitates the development of an advanced electrolyte system characterized by decent ionic conductivity, effective interphase formation, and a wide electrochemical window.[1]

Interphases, including solid electrolyte interphase (SEI) on the anode and the cathode electrolyte interphase (CEI) on the cathode, are critical components for achieving optimal battery performance.[2] Since most electrolytes are unstable during electrochemical cycling, their decomposition products accumulate on the electrodes, forming these interphases. The formed interphases act as protective layers, preventing continuous electrolyte decomposition while still allowing lithium-ion transport. Effective and stable interphases should stabilize the electrodes and mitigate side reactions between the electrolyte and electrodes. The practical application of graphite electrodes was only realized after the introduction of ethylene carbonate into the electrolyte, highlighting the importance of SEI. Similarly, the high energy density, lithium metal anode based batteries have become increasingly successful which is enabled by electrolyte and interphase optimization.[3-6] On the cathode side, a robust CEI is crucial for enabling the use of high energy density Ni-rich cathodes, as it prevents or suppresses electrolyte oxidation on the highly catalytic cathode surface. In addition, a good CEI mitigates structural degradation, crack formation, and transition metal dissolution.[7-9] The significance of SEI and CEI becomes even more pronounced under extreme conditions, such as high voltage, fast charging, and wide temperature ranges.[10-14] In these scenarios, not only is the stability of the interphase critical, but its resistance also plays a key role in enhancing battery kinetics. Consequently, optimizing interphases through electrolyte development has become a primary focus in efforts to improve overall battery performance.[15]

Current electrolyte design strategy emphasizes achieving anion-derived interphases to obtain long cycle life. One example of this is the development of solvent-in-salt, or high concentration electrolyte (HCE) and localized high concentration electrolyte (LHCE), where the high salt concentration compels anions to appear in the solvation sheath, contributing to interphase formation[16-18]. The efficacy of this method is evident in many successful electrolyte systems designed based on this strategy[19, 20]. Another approach to obtain anion-derived interphases involves weakening solvation strength by fluorinating the solvent, as seen in fluorinated ethers[21-23]. The resultant weaker solvation between Li^+ and the solvent allows anions to be part of the solvation sheath, thereby promoting the formation of an anion-derived interphase.

The strategy of using anion-derived interphases has been shown to effectively enhance battery cycle life. However, this often comes at the expense of other important properties, particularly ion transport kinetics. In HCE and LHCE

electrolytes, the increased ion pairs and aggregates plays a crucial role in developing anion-derived interphases. However, these same factors also significantly increase electrolyte viscosity and reduce ionic conductivity. The ionic conductivity of LHCE typically ranges from 1 to 2 mS cm^{-1}, while HCE features even lower values. This poor bulk ionic conductivity severely limits ion transport, particularly under extreme conditions, leading to unsatisfactory performance under demanding conditions like fast charging and operation at low temperatures.[19, 24, 25] To develop an electrolyte capable of meeting stringent requirements simultaneously—including fast charging, operation across a wide temperature range, and extended cycle life—new electrolyte design strategies need to be explored.

We propose designing an electrolyte system that leverages both solvents and anions to form interphases, moving beyond the conventional reliance on anions alone. This approach broadens the selection of potential solvents, including those with superior ionic conductivity. Linear carbonates, for instance, are appealing due to their low viscosity, low volatility, and cost-effectiveness. In the literature, there were various studies exploring the use of linear carbonate as the major solvent for lithium-ion batteries[26-29]. Some approaches are on introducing additives such as $LiNO_3$, fluoroethylene carbonate (FEC), vinylene carbonate (VC), 1,3,2-Dioxathiolane-2,2-dioxide (DTD) to address the interphase problem common in linear carbonates.[29] Efforts have also been made to develop HCE or LHCE using linear carbonates.[27, 30, 31] Some recent attempts include fluorinating the linear carbonate to tailor the solvation strength, which has been believed to facilitate ion desolvation and interphase transport kinetics.[32, 33] This study also concluded that partial fluorination in some cases results in better cycling stability compared to full fluorination that was attributed to locally-polar $–CH_2F$ and $–CHF_2$ groups in accord with the analogous study on the ester-based electrolyte.[34] Importantly, ester electrolyte with the $-CF_2H$ group showed the best low temperature performance.

In this work, we designed a new electrolyte system using linear carbonate as the major solvent and our strategy is based on the idea of using both solvent and anion to form the interphases. To balance the ion solvation strength and interphase formation capabilities, we introduce locally polar $-CHF_2$ group into diethyl carbonate, leading to a new solvent—2,2-difluoroethyl ethyl carbonate (DFDEC). The DFDEC-based electrolyte has sufficient ionic conductivity to support fast charging and low temperature operation. The relatively high boiling point of DFDEC also makes it possible to operate LIB at high temperature as well. More importantly, experimental and theoretical studies suggest both DFDEC solvent and bis(fluorosulfonyl) imide (FSI) anion contribute to the interphase formation on anode and cathode, validating our design strategy. The combined merits of DFDEC-based electrolyte enable LIB under extreme conditions such as fast charging, low and high temperature operation, and long cycle life.

RESULTS AND DISCUSSION

As discussed previously, departure from the reliance of anion to form the interphases gives access to a larger scope of solvent choices, potentially enabling the LIBs to operate satisfactorily under various demanding conditions (Figure 1a). It should be noted that solvent-derived interphase is not necessarily always inferior to the anion-derived one. For example, ethylene carbonate (EC) derived interphase is the key enabler for graphite-based LIB under normal conditions.[35] However, its high viscosity prevents its usage under demanding conditions such as fast charging and low temperature operation. Diethyl carbonate (DEC) is a widely used electrolyte co-solvent because of its low freezing point and low viscosity. Its weak interaction with Li also facilitates the Li desolvation process.[36] However, DEC alone is not able to form a stable interphase on the electrode, resulting in solvent co-intercalation and battery failure. To go beyond, it is necessary to identify other solvents with balanced interphase formation capability and transport property. In this work, partially fluorinated diethyl carbonate (DFDEC) which has two fluorine atoms on one ethyl end (Figure 1b) is chosen as the solvent. Compared to fully fluorinated compounds, partial fluorination allows not only stronger interaction with Li but also coordination with the anions and solvent oxygens owing to the local dipole, therefore resulting in balanced ion transport and interphase properties.[21, 32, 37, 38] Fluorinating DEC significantly improves the reversibility of charge-discharge as shown in Figure S1, suggesting the much-improved interphase. To design an electrolyte meeting all demanding requirements, lithium bis(fluorosulfonyl) imide (LiFSI) is chosen over $LiPF_6$ because of the former has higher temperature stability, higher solubility, as well as better interphase forming capability.[39] Further optimization of the salt concentration (Figure S2) leads to electrolyte consisting of 2M LiFSI in DFDEC with FEC additive (denoted as "FLC") with satisfactory performance under various extreme conditions. To demonstrate the performance improvement and the distinct interphase formation of FLC electrolyte, commercial LP40 electrolyte (1M $LiPF_6$ in EC/DEC, 1/1, wt%) is used as baseline electrolyte for comparison.

The electrochemical stabilities of FLC and LP40 electrolytes were evaluated and compared. Cyclic voltammetry (CV) in Li||graphite cells were measured to understand the stability of electrolytes on graphite anodes. As shown in Figure 1c, reversible Li intercalation/de-intercalation in the graphite is observed in both electrolytes. In LP40, the reduction peak at 0.67 V is primarily due to EC decomposition[40, 41]. In the FLC electrolyte, a broad reduction peak at 1.25 V with an onset of approximately 1.8 V is observed (inset graph of Figure 1c). Linear swipe voltammetry (LSV) is carried out in Li||Al cells to understand the oxidative stability of the electrolyte and the results are shown in Figure 1d. Compared with LP40, FLC has a higher decomposition onset voltage and a lower response current, suggesting its superior oxidation stability.

To understand the solvation structure and transport of both LP40 and FLC electrolytes, molecular dynamics (MD) simulations were implemented.[42] The predicted structure factor S(Q) and ionic conductivity from MD for both LP40 and FLC electrolytes are in excellent agreement with experiments as shown in Figure S3 and Figure 1e. The predicted self-diffusion coefficients from MD simulations for LP40 electrolyte are also in good agreement with the interpolated NMR data from Hayamizu as shown in Table S1.[43] For LP40, MD prediction and experimental results

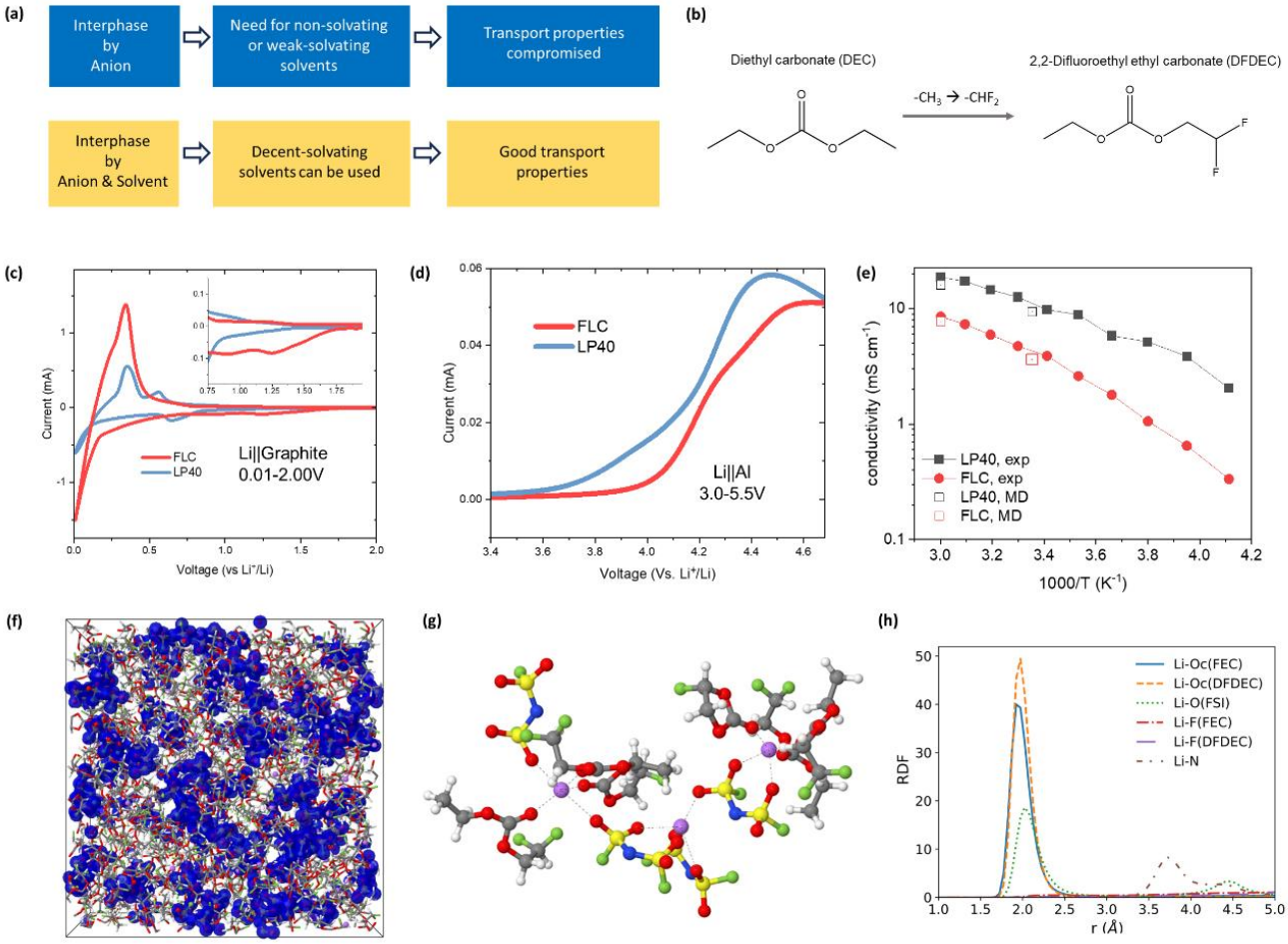

Figure 1. (a) Electrolyte design strategies. (b) Molecular structures of DEC and DFDEC. (c) Cyclic voltammetry (CV) curves of Li||graphite cell using FLC and LP40 electrolytes. (d) oxidation stability window of FLC and LP40 electrolytes. The error in the measured CV voltage is better than 1mV and in current less than 1μA. (e) Conductivity of LP40 and FLC electrolytes from experiments and MD simulations at 298 K. (f) Snapshots of MD simulations boxes for FLC electrolytes with solvents show as wireframe and anions highlighted with blue isosurfaces. (g) Representative Li^+ solvates from MD simulations of FLC electrolytes at 298 K. (h) Radial distribution functions for FLC electrolyte with a focus on the Li^+ environment. Carbonate oxygen atoms are denoted as Oc, non-carbonate oxygens as EO.

agree well on the degree of correlated ionic motion (ionicity) with MD being 0.58-0.63 and experimental measurement being 0.6.[43] It is noted that such agreement is reached without empirical adjustments or charge scaling typical for non-polarizable force fields[10], validating the force field used in MD and the reliability of the simulation results. The lower ionic conductivity of FLC electrolyte is attributed to more extensive ionic aggregation confirmed by MD simulations (Figures S4, 1f). Interestingly, similar ionicity values of 0.55-0.63 and transference numbers in the center of mass frame (t_+^{COM}) around 0.31-0.37 were extracted for LP40 and FLC (Figure S5) despite different states of ion aggregation. This is due to relatively fast exchange between the Li^+ cations and FSI^- anions contributing to ion transport in a more concentrated FLC electrolyte. A representative Li^+ solvate in FLC electrolyte from MD simulation is shown in Figure 1g, illustrating the presence of FSI^- anion, DFDEC solvent, and FEC additive in the vicinity of Li^+ cation. Radial distribution functions (RDFs) (Figure 1h, Figure S6) of FLC electrolyte showed that Li^+-Oc(DFDEC) first peak is the highest followed by Li^+-Oc(FEC) and Li^+-Oc(FSI). A Li^+ cation is coordinated to 2.13 DFDEC, 1.11 FSI^- anions, and 0.88 FEC. Such solvation structure suggests that both DFDEC solvent and FSI^- anion will make significant contributions to the interphases, which is the core idea of electrolyte design in this work. In LP40, Li^+ has the highest affinity to carbonyl oxygen from EC followed by carbonyl oxygen from DEC and fluorine from PF_6^- anions. That is, a Li^+ cation is coordinated by 2.22 EC, 1.39 DEC and 0.57 PF_6^- anions. The influence of the local dipole induced by -CHF_2 group was examined using RDFs (see Figure S7). They show that F from the -CHF_2 group of DFDEC has the highest first shell Li–F coordination peak around 2.3 Å compared to the Li-F(FEC) and Li-F(FSI). Such direct Li-F contact facilitates the LiF formation as a result of reduction of the Li+(DFDEC) discussed below. Importantly, compared with the -CHF- group of FEC and -CH_3 group of DFDEC, the polar -CHF_2 group interacts with both O(FSI^-) anion and O(FEC). This is indicated by the strong peaks in Figure S7(b) (marked by red box), which

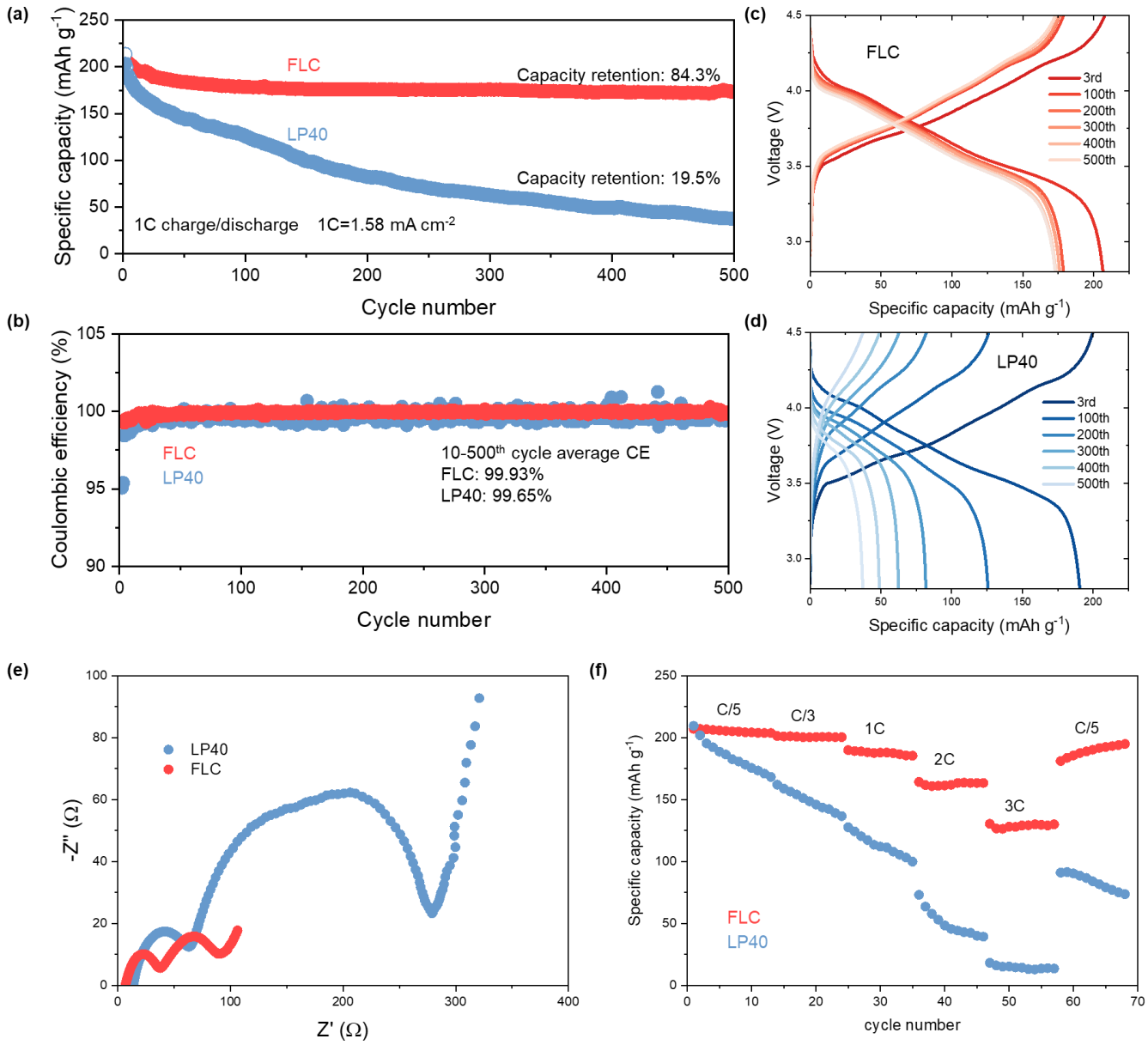

Figure 2. Electrochemical performance of Gr||NMC811 cells. (a) Long-term cycling stability and (b) Coulombic efficiency at 1C within the voltage range of 2.8 V to 4.5V. Voltage profiles of the cells using (c) FLC and (d) LP40 electrolytes. (e) EIS spectra after 500 cycles. (f) Rate capability of the cells using FLC and LP40 electrolytes.

correspond to H of -CHF_2 interacting with O of FSI^- anion and carbonyl oxygen of FEC. In comparison, the H from -CHF group and from -CH_3 group has weaker interactions with FSI^- anion or/and cosolvent as indicated by Figure S7(c-d). The importance of tailoring the strength of the intermolecular $F^{\delta-}$–$H^{\delta+}$ or $H^{\delta+}$–$O^{\delta-}$ bonds to adjust solvent-salt interaction, salt solubility and Li^+ desolvation was recently highlighted.[44] The different solvation structures in LP40 and FLC electrolytes is expected to lead to distinct interphase formation mechanisms in two electrolyte systems which will be elaborated later when we discuss the interphases.

The electrochemical performance was evaluated in the graphite||NMC811 full cells. Both graphite anode and NMC811 cathode are characterized by XRD and SEM (Figures S8-S11), revealing their crystal structure, purity, and morphologies. When the cutoff voltage is 4.4 V, the full cell using FLC electrolyte delivered close to 200 mAh g^{-1} initially and still has around 196 mAh g^{-1} capacity after 600 cycles, corresponding to a capacity retention of 99.5% (Figure S12). It is noted that a fast rate of 1C charge-discharge was used. The FLC electrolyte also demonstrates excellent capacity retention even when the charge voltage is increased to 4.5 V. Figure 2a and 2b show that at 1C charge-discharge rate, the 4.5 V full cell using the FLC electrolyte

has a capacity retention of 84.3% after 500 cycles, with an average coulombic efficiency (CE) of 99.93%. In comparison, the graphite||NMC811 cell using LP40 electrolyte only retains 19.5% of its initial capacity, with an average CE of 99.65%. Figure 2c and 2d display the charge and discharge curves at selected cycles. The voltage profiles of the cell using FLC is highly reversibly while that of the cell using LP40 has rapid capacity decay and fast overpotential buildup. Although FLC achieved much better stability over cycling, the average CE of 99.93% still suggests irreversible Li^+ loss probably owing to electrolyte electrode side reactions. Therefore, for beyond the tested cycles, possible degradation still could happen.[45] The electrode/electrolyte side reactions consumes both electrolyte and available Li ions in the battery system, leading to interphase accumulation and impedance buildup. Eventually, the battery fails when there is no available Li^+ and electrolyte over extended long-term cycles.

Electrochemical impedance spectroscopy (EIS) was utilized to evaluate the impedance characteristics of the batteries after cycling, as shown in Figure 2e. The analysis revealed that both the interphase resistance (indicated by the high frequency semicircle) and the charge transfer resistance (indicated by the middle frequency semicircle) are significantly reduced in the cell employing the FLC electrolyte compared to the LP40 electrolyte. This reduction indicates a more ionically conductive interphase and an enhanced protection of the cathode surface in the FLC electrolyte scenario. Notably, the charge transfer resistance, represented by the second semicircle, is remarkably higher for the LP40 electrolyte than for the FLC electrolyte. This observation suggests that the cathode in the cell using LP40 electrolyte may be prone to severe surface reconstruction, which is usually associated with the reduction and dissolution of transition metals. Further support for this argument is provided by subsequent surface and interphase characterizations. Figure 2f showcases a comparison of the rate performance between the two electrolytes. As the current density increases, the capacity of the cell using LP40 electrolyte significantly deteriorates, with difficulty in capacity recovery even when the current density is reduced back to C/5. This is likely due to irreversible processes such as lithium plating on graphite at high current densities. In contrast, the cell using FLC electrolyte can still deliver a capacity as high as 130 mAh g^{-1} at a 3C rate, with the ability to recover most of the low rate capacity upon reducing the current density. Despite the FLC electrolyte exhibiting lower electrolyte bulk ionic conductivity compared to LP40 (Figure S13), its superior overall cell rate performance suggests that it has significantly lower interphase impedance.

The success of FLC electrolyte hinges on its capability to form interphases with contributions from both anion and solvent. The electrolyte-graphite interphase is characterized both theoretically and experimentally. DFT calculation indicates DFDEC makes significant contribution to forming stable interphase on graphite anode (Figure 3a). When Li···F(FEC or DFDEC) close contact is present in a solvate, reduction will occur in the potential range from 1.4 V to 1.8 V. This DFT prediction is in excellent agreement with the experimental CV study discussed in Figure 1, where a broad reduction peak starting from 1.8V is observed. Because Li···F(DFDEC) contacts are 15 times more frequent than Li···F(FEC) contacts, Li^+(DFDEC) reduction is expected to contribute to this reduction process much more than Li^+(FEC) reduction. Previous calculations reported Li^+(FEC) reduction without LiF formation for the reduction peak at 0.9V.[41] FEC reduction without LiF formation were observed at 0.89 V and 1.07 V as shown in Figures S14 and S15 for the $Li^+(FEC)(DFDEC)_3$ and $Li^+(FEC)_2(DFDEC)_3$ model solvates, respectively. This change indicates the influence of solvate packing on reduction potential. Anion FSI plays a relatively minor role in interphase formation on graphite anode, with a weak current at around 1.6 V contributed by contact ion pairs.

To understand the improved electrochemical performance in FLC electrolyte, post-mortem analysis of the cycled graphite anode and NMC811 cathode in both LP40 and FLC electrolyte was performed. X-ray photoelectron Spectroscopy (XPS) measurements provide surface composition information. Taking advantage of the synchrotron XPS with tunable incident X-ray energies ranging from 2000 eV to 5000 eV, the interphase composition at different depths is obtained. In the FLC electrolyte (Figure 3b), C=O and O-C=O molecular moieties arising from DFDEC solvent decomposition are observed in the O 1s spectra. The F 1s spectra (Figure 3c) indicate the fluorine-containing species are mostly LiF which should be mostly generated by solvent decomposition. Although FEC decomposition can also form LiF[46], the significantly higher Li···F(DFDEC) contacts in the FLC electrolyte suggest that LiF is primarily formed by DFDEC. At the low depth corresponding to the side of interphase close to the electrolyte, small amounts of S-F containing species are detected, likely resulting from anion decomposition or residue salt in the FLC electrolyte. The unchanged oxygen and fluorine XPS results, regardless of changes in incident X-ray energy, suggests that oxygen- and fluorine-containing species are uniformly distributed within the electrolyte-graphite interphase when the FLC electrolyte is used. This uniform SEI layer on the graphite anode, composed of organic carbonate species and inorganic LiF, effectively inhibits electrolyte decomposition and stabilizes graphite anode. Due to EC decomposition, the SEI formed in the LP40 electrolyte contains solvent-derived carbonates as indicated by the C=O and O-C=O peaks in the O 1s spectra. These species are uniformly distributed within the SEI layer, with no significant variation at different depths. The F 1s spectra suggest that PF_6 anions also make considerable contributions to the SEI formation, probably due to the instability of $LiPF_6$ salt that is prone to self-decomposition. These observations are consistent with previous studies of LP40 electrolyte.[40] As a result of residual salt, large quantities of $LiPF_6$ accumulate at the top of the SEI, while its decomposition products ($Li_xPO_yF_z$, LiF)[47] reside deeper in the interphase which is closer to the graphite.

The cycled graphite electrodes were also analyzed using scanning electron microscopy (SEM) and elemental dispersive (EDS) mapping. Figure S16 compares the morphology of graphite after 500 cycles. The graphite anode cycled in the FLC electrolyte exhibits a more uniform and smoother surface, indicating better compatibility and reduced side

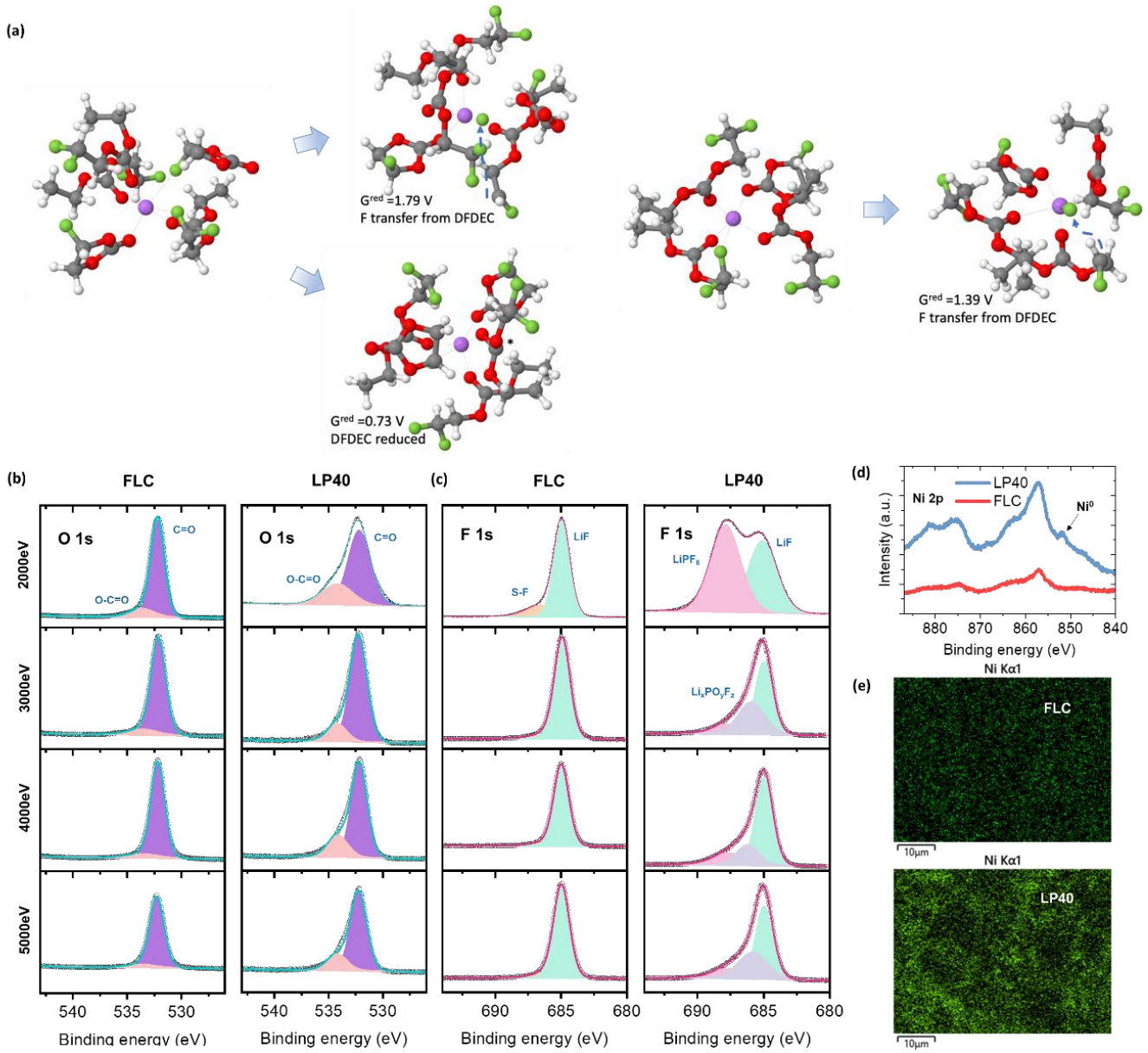

Figure 3. (a) Reduction potentials vs. Li/Li^+ for $Li^+(FEC)_2(DFDEC)_3$ and $Li^+(FEC)(DFDEC)_3$ solvates from ωB97XD/6-31+G(d,p)/PCM(ε=20) DFT calculations. Asterisk indicated the reduced DFDEC specie. XPS results of cycled graphite anode. XPS spectra of (b) O1s and (c) F 1s on cycled graphite in FLC and LP40 electrolytes. (d) Ni 2p spectra of cycled graphite anode with incident X-ray energy of 2000 eV. (e) Ni EDS mapping of cycled graphite anode in LP40 and FLC electrolytes. The error in the measured XPS intensity is better than 1% and in photon energy better than 0.05 eV.

reactions at the graphite electrode compared to the case of the LP40 electrolyte. EDS mapping, which provides detailed information on the concentration and distribution of different elements, reveals a higher concentration and more uniform distribution of fluorine species on the graphite surface when using FLC electrolyte (Figure S16). In contrast, when cycled in LP40, there is less fluorine species due to limited salt decomposition. Fluorine species especially LiF has been widely accepted as beneficial and protective interphase components.[48-50] The higher abundance of them in the SEI formed in FLC electrolyte lead to better passivation of graphite anode compared with the LP40 electrolyte. In addition, owing to SEI degradation after long-term cycles in LP40, regions with minimal or no SEI coverage are observed on the cycled graphite, as indicated by the black regions marked in the mapping. These exposed areas render the graphite electrode more susceptible to side reactions with the electrolyte, leading to the consumption of both the electrolyte and lithium ion reservoir. Consequently, prolonged cycling in LP40 electrolyte leads to significant impedance increase and capacity decay. High voltage battery cycling can easily cause transition metal dissolution. The dissolution and its deposition on the graphite anode degrades SEI and the long-term battery performance. Based on the Ni 2p XPS results in Figure 3d, obvious Ni signals are observed in the cycled graphite in LP40 electrolyte. Additionally, the lower energy peak located at around 852 eV suggests the presence of low

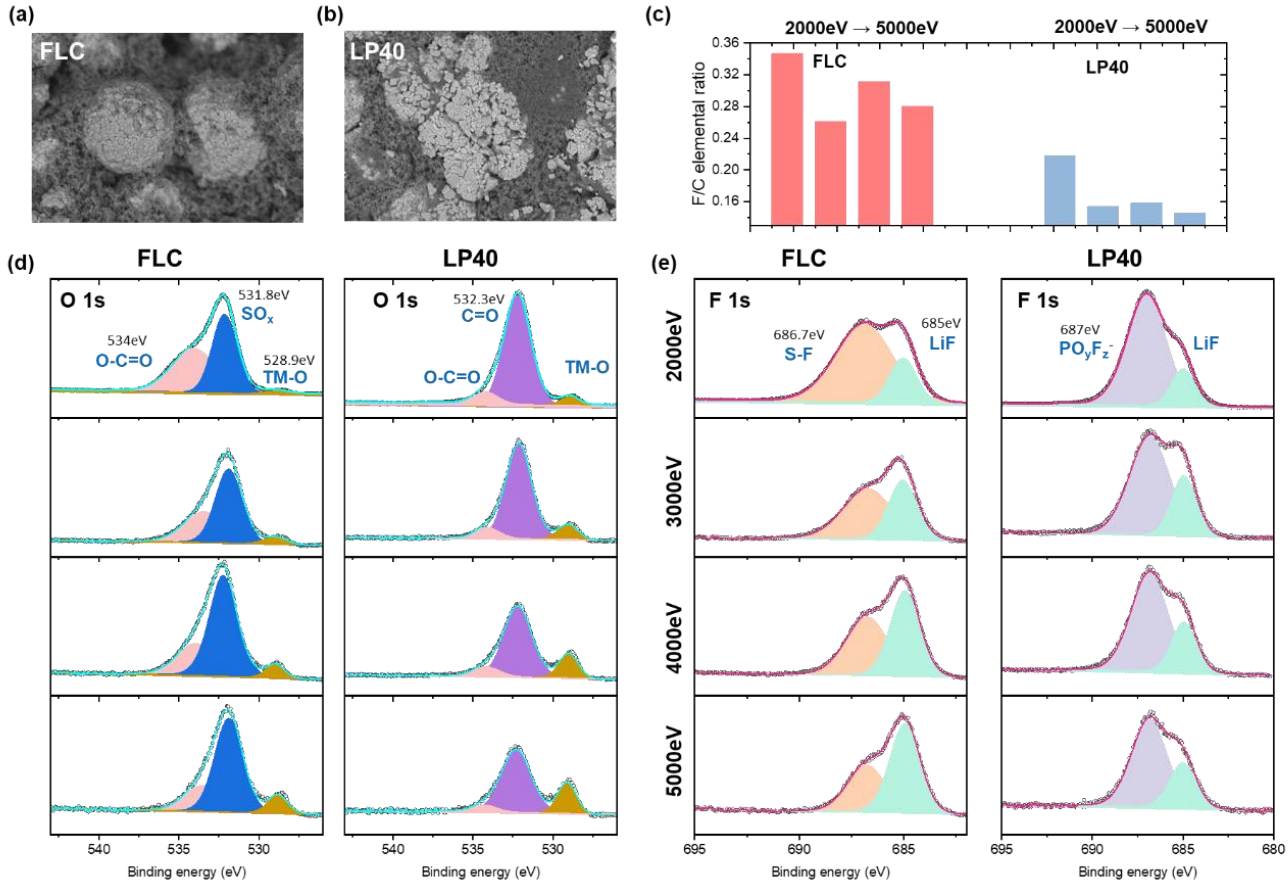

Figure 4. SEM images of cycled NMC cathode in (a) FLC and (b) LP40 electrolytes. (c) Fluorine to carbon element ratio on cycled NMC cathode from XPS measurements. XPS spectra (d) O1s and (e) F 1s on cycled NMC in FLC and LP40 electrolytes. The error in the measured XPS intensity is better than 1% and in photon energy better than 0.05 eV.

valence state Ni species (i.e., Ni^0) on the anode surface. The amount and distribution of the Ni signals are further verified using EDS mapping in Figure 3e. Less Ni signals are observed in the cycled graphite anode in FLC electrolyte, suggesting suppressed transition metal dissolution.

Continuous long-term cycling at high voltage usually causes strain buildup in the cathode, resulting in crack formation, which further accelerates the electrolyte and electrode side reactions because of more exposed fresh cathode surfaces. According to the SEM images of the cycled NMC811 electrode in Figure 4a-b and Figure S17, using the FLC electrolyte sufficiently suppressed the NMC811 crack formation. To understand the CEI formed in the FLC and LP40 electrolytes, XPS measurements were performed. Owing to the fluorinated solvents and FSI salt in FLC electrolyte, high abundance of fluorine species in the CEI is observed as suggested by the higher fluorine/carbon elemental ratio shown in Figure 4c. The narrow carbon scan results (Figure S18) reveal similar carbon species formed in these two electrolytes, consisting of conductive carbon (C-C/C-H) and solvent decomposition species (C-O, C=O). C-F signal is attributed to PVDF binder or fluorinated solvent. Detailed fluorine species analysis is in shown Figure 4e. The FLC electrolyte promotes an interphase consisting of S-F and LiF because of FSI^- decomposition. With the increasing of X-ray energies, the LiF gradually becomes the dominant component, owing to more complete decomposition of FSI^- closer to the NMC811 surface. The dominance of LiF formed in the FLC electrolyte suggests better and more protective CEI formation. In the LP40 electrolyte, the fluorine signal is composed of $PF_yO_z^-$ and LiF due to salt $LiPF_6$ decomposition,[51, 52] the $PF_yO_z^-$ is always the major phase at different X-ray energies. Oxygen XPS of the CEI formed in the FLC electrolyte (Figure 4d) has three peaks corresponding three different chemical species: SO_x species from LiFSI decomposition,[20, 53] O-C=O species from solvent/additive decomposition, and TM-O from bulk NMC811. As the incident X-ray energy increases, SO_x peak becomes more prominent, indicating more complete FSI decomposition at the deep layers of the interphase, where electron is more accessible compared to the surface layers of the interphase. The dominance of SO_x peak and the relatively weak carbon signals indicate that the CEI in the FLC electrolyte is mainly composed of LiFSI decomposition products (LiF, SO_x, etc)[54]. FSI^- anion decomposition also generates sulfur species in the CEI (Figure S19). The uniform fluorine and sulfur species distribution on the NMC811 surface in Figure S20 suggests that the FSI derived CEI is uniformly covering and protecting cathode surface. In LP40 electrolyte, the high carbon amount suggests that the CEI is mostly derived from solvent decomposition, generating C=O and O-C=O species observed in Figure 4d. The TM-O peak in oxygen XPS originates from bulk

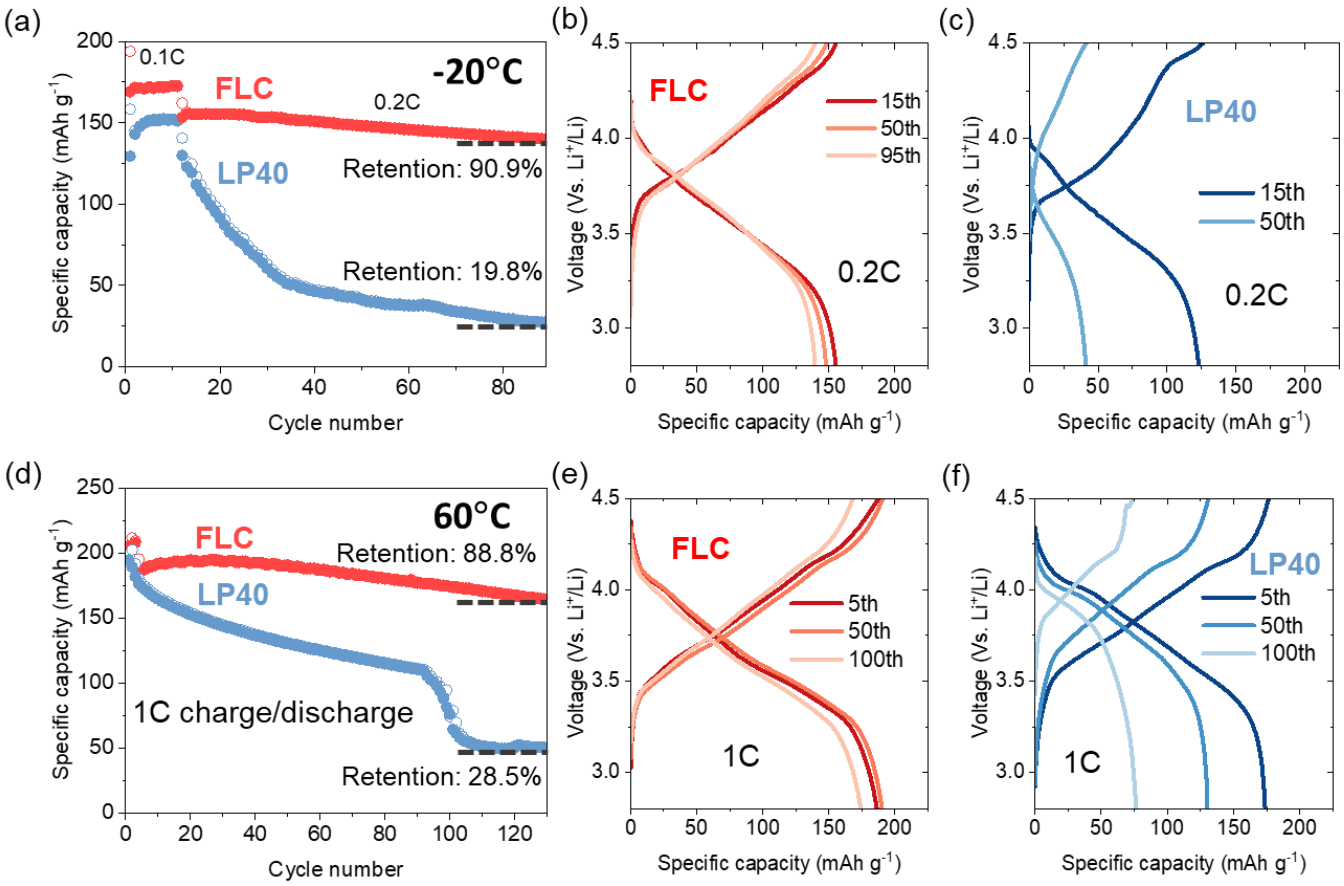

Figure 5. Electrochemical performance of Gr||NMC811 cells at different temperatures. (a) Long-term cycling stability at -20 °C. Voltage profiles of the cells cycled at -20 °C using (b) FLC and (c) LP40. (d) Long-term cycling stability at 60 °C. Voltage profiles of the cells cycled at 60 °C using (e) FLC and (f) LP40.

NMC811. At 2000 eV, compared with the LP40 electrolyte, the smaller TM-O signals in the FLC electrolyte suggest a thicker CEI formation or a better coverage CEI on the cathode surface. This salt derived LiF-rich interphase formed in the FLC electrolyte enables a more protective CEI on the NMC811 cathode at high voltage, suppressing transition metal dissolution and crack formation after long-term cycling.

SEI and CEI studies highlight the synergistic effects of DFDEC solvent and LiFSI salt in forming robust interphases and enhancing electrochemical performance in FLC electrolyte. FEC is well known to have good interphase formation capabilities. To understand its role in the FLC electrolyte, we performed comparison studies in various electrolyte systems. First, a comparison is made between 1M $LiPF_6$ in DFDEC electrolyte and 1M $LiPF_6$ in DFDEC/FEC (volume ratio 9:1) electrolyte. As Figure S21(a) suggests, the cell using 1M $LiPF_6$ in DFDEC electrolyte experiences rapid capacity decay. Adding FEC improves the cycle life, which is suggested by Figure S21(b) showing the data of cell using 1M $LiPF_6$ in DFDEC/FEC. However, such improvement is limited as the capacity decays to ~70% of its initial value after 200 cycles. This case study indicates without a proper salt, FEC is not able to deliver high performance. Similarly, another comparison is made between 2M LiFSI in DEC/FEC electrolyte and FLC electrolyte (the only difference is the major solvent which is DEC in the former and DFDEC in the latter) and the results are shown in Figure S22. It suggests that without a proper major solvent, FEC cannot promise long cycle life. These comparisons indicate that while FEC has beneficial effect on forming good interphases and extending cycle life, its role is limited in the FLC electrolyte. The superior performance of FLC electrolyte is attributed to the synergistic effect of LiFSI salt and the DFDEC solvent, leading to LiFSI-derived CEI and DFDEC-derived SEI. Combing DFT calculation and XPS characterizations, DFDEC decomposition promotes carbonate and LiF-rich SEI on graphite anode, uniformly covering the anode surface and preventing side reactions. On the NMC811 surface, LiFSI generates S-F and LiF-rich CEI, inhibiting further electrolyte oxidation and NMC degradation (i.e., cracking, transition metal dissolution, etc.).

The stable and ionic conductive interphases formed in the FLC electrolyte enable the superior electrochemical performance at more extreme cycling conditions and environmental temperatures. In Figure S23, at a current density of 2C and high cutoff voltage of 4.5 V, the cell delivers a high capacity of 188 mAh g^{-1} at 5th cycle. Because of constant current constant voltage cycling protocol, the delivered capacity is larger than the value obtained in the rate capability test. With the increasing of cycle number, capacity decay and polarization are observed. After 300 cycles (Figure S23), the graphite||NMC811 full cell delivers

77.7% of its initial capacity, with a high average CE of 99.81%. When the current density is increased to 3C, the full cell still delivers 135 mAh g^{-1} capacity after 300 cycles as shown in Figure S24.

Full cells operating at low temperature and high temperature are also tested. At -20 °C (Figure 5a, Figure S25), the FLC electrolyte delivers 171 mAh g^{-1} capacity at 0.1C and 156 mAh g^{-1} at 0.2C. After 90 cycles at 0.2C, the cell still delivers 141 mAh g^{-1} capacity, with 90.9% capacity retention. However, in the LP40 electrolyte, the full delivers 151 mAh g^{-1} capacity at 0.1C, and experiences fast capacity decay at 0.2C for the longer cycles. The charge and discharge curves in Figure 5b, 5c further confirm the stable cycling behavior in the FLC electrolyte with minimum overpotential change, while there is rapid overpotential growth and capacity loss in LP40 electrolyte owing to the decreased cell kinetics at low temperature. As confirmed by EIS results (Figure S26), significantly higher interphase and charge transfer resistance in LP40 electrolyte greatly impede ion transport at -20 °C, leading to capacity drop and large polarization. Besides low temperature operation, FLC electrolyte enables stable cycling at high temperature as well. The 4.5 V graphite||NMC811 full cell using FLC electrolyte delivers a capacity of 205.4 mAh g^{-1} at 1C at 60 °C. After 130 cycles (Figure 5d), the cell delivers a high capacity of 164 mAh g^{-1}, retaining 88.8% of its initial capacity. As for the cell cycling in LP40 electrolyte, the initial discharge capacity is slightly lower (194.4 mAh g^{-1}). After 130 cycles, the capacity drops quickly, only remaining 28.5% of initial capacity afterwards. The charge and discharge profiles from selected cycles are displayed in Figure 5e and 5f. The stable curve with minimum polarization is achieved when using the FLC electrolyte, while the capacity decay and overpotential growth are observed when the LP40 electrolyte is used. The superior high temperature electrochemical performance of FLC electrolyte can be attributed to several factors. First, LiFSI, which has better thermal stability than $LiPF_6$, is used as the salt in the electrolyte. The slightly higher salt concentration of 2M in the FLC electrolyte further enhances thermal stability and reduces volatility.[55] More importantly, DFDEC decomposition promotes carbonate and LiF-rich SEI on graphite anode, while LiFSI generates S-F and LiF-rich CEI on NMC811 cathode.[56] These inorganic species-rich interphases effectively inhibit side reactions at elevated temperatures, contributing to the improved performance of the FLC electrolyte under high-temperature conditions.

Among the various high-performance wide-temperature electrolytes reported (Figure S27 and Table S2),[17, 27, 57-63] the FLC electrolyte also shows great potential as a promising candidate for practical applications across a wide temperature range.

CONCLUSIONS

In this work, we propose a new electrolyte design strategy which encourages both solvent and anion to contribute to the interphase formation. Such strategy enables the selection of solvents with good ion transport properties and can potentially enable LIBs to operate under extreme conditions such as fast charging, low and high temperatures. Based on this idea, partially fluorinated linear carbonate-2,2-difluoroethyl ethyl carbonate is chosen as a new and major solvent for the electrolyte system FLC. Its synergy with LiFSI salt led to graphite-electrolyte interphase that is formed mostly by solvent and cathode-electrolyte interphase that is formed mostly by anion. Therefore, the graphite||NMC811 cells using FLC electrolyte achieved super stable long-term cycling, with a capacity retention of 99.5% after 600 cycles within a voltage range of 2.8 V to 4.4V, and a capacity retention of 84.3% after 500 cycles within a voltage range of 2.8 V to 4.5 V. Full cell electrochemical performance at extreme cycling conditions is also greatly enhanced by using the developed FLC electrolyte. After cycling at 2C within 2.8 V to 4.5V, the graphite||NMC811 cell still delivers 77.7% of its initial capacity. Additionally, the new electrolyte also promotes battery operation within a wide temperature range (-20 °C to 60 °C) with greatly improved capacity retention and substantially suppressed polarization growth.

EXPERIMENTAL METHODS

Electrolyte and electrode preparation: All the electrolytes were prepared inside the Argon filled glovebox with controlled oxygen and water level. The conventional electrolyte LP40, 1 M $LiPF_6$ in ethylene carbonate (EC) – diethyl carbonate (DEC) (1:1 by weight) is used as baseline electrolyte. The FLC electrolyte was prepared by dissolving 2.0M LiFSI (Nippon Shokubai) in the mixture of FEC (Oakwood chemical) and DFDEC (SynQuest Labs), the volume ratio between FEC and DFDEC is 1:4. The water content is measured by Karl Fischer titration (Metrohm Eco Coulometer) to be 15-20 ppm. Graphite and NMC811 electrodes were obtained from the Cell Analysis, Modeling, and Prototyping (CAMP) Facility at Argonne National Laboratory (ANL). Graphite anode is composed of 91.83 wt% superior graphite SLC1520P, 2wt% Timcal C45 carbon, 6wt% Kureha 9300 PVDF binder and 0.17 wt% oxalic acid. NMC811 cathode consists of 90wt% NMC811, 5wt% Timcal C45 and 5wt% Solvay 5130 PVDF binder. The areal loadings of graphite and NMC811 electrodes are 1.8 mAh cm^{-2} and 1.58 mAh cm^{-2}, respectively. The graphite and NMC811 electrodes were punched into electrode discs with a diameter of 12.7 mm, dried under vacuum overnight, and transferred to the glovebox before use.

Electrochemical measurements: The 2032-type coin cells were used for electrochemical measurements. The graphite||NMC811 cells were assembled inside the Ar-filled glove box, using one piece of NMC811 disc as cathode and one piece of graphite as anode sandwiched by Celgard 2320 separator and 40 μL electrolyte. For the galvanostatic cycling, the graphite||NMC811 cells were cycled at 0.1C for 2 cycles, followed by 1C (1C = 1.58 mA cm^{-2}) for the rest of the cycles within the voltage range between 2.8 V and 4.5 V. For the rate capability test, two formation cycles at 0.1C were performed first, followed by rate tests in the same voltage range. The high rate cycling measurements were carried out using the constant current constant voltage (CCCV) protocol for both charging and discharging process. The cutoff current for the CCCV protocol is 0.2C for the 2C cycling and 0.3C for the 3C cycling. All the room temperature battery cycling has been performed in the building with controlled temperature (70 °F) and humidity (50-55%). For the low or high temperature cycling, 2 formation

cycles at 0.1C at room temperature were carried out, followed by long-term cycling at -20 °C or 60 °C in the Tenney temperature chamber with temperature uncertainty within 1°C.

The anodic cyclic voltammetry tests were carried out from 3.0 V to 5.5 V in Li||Al cells, at a scan rate of 1 mV s^{-1}. The errors in voltage and current measurements are better than 1mV and 1 μA, respectively. For the ionic conductivity test, it was measured inside Pt||Pt symmetric cells on a Biologic SP-300 system. The EIS measurements for the cycled cells were performed over a frequency range of 7 MHz to 1 mHz at controlled temperatures using the Tenney test chamber. The solution resistance at various temperatures was obtained, and it can be converted to ionic conductivity using the following equation:

$$R = \rho \frac{l}{A}$$

where *l* is the distance between the electrodes, *A* is the Pt electrode area, *R* represents the solution resistance, and ρ is the resistivity. The reciprocal of resistivity is the ionic conductivity. To obtain the *l* and *A*, a standard solution KCl was used. There might be errors in the measurements which may mainly come from electrode area and distance between Pt electrodes. To ensure high accuracies, we performed test for standard solution multiple times. In addition, ionic conductivity measurements for the electrolytes are also performed more than once to improve the accuracy.

Characterizations: The morphology of the cycled electrode was characterized by scanning electron microscopy (Hitachi 4800) at the Center for Functional Nanomaterials (CFN) of the Brookhaven National Laboratory (BNL). The energy dispersive spectroscopy (EDS) characterization of cycled electrode was carried out using JEOL JSM-7600F at CFN.

The hard X-ray photoelectron spectroscopy (HAXPES) measurement was carried out at the National Institute of Standards and Technology beamline 7-ID-2 of National Synchrotron Light Source (NSLS) II at BNL. Samples were transferred to the beamline under Argon gas and introduced into the vacuum chamber to minimize exposure to air. The cycled NMC811 electrodes were mounted onto sample holder after washing and drying. Photon energy selection was obtained using a double-crystal monochromator. Measurements were made with a 400 mm diameter hemispherical electron analyzer mounted perpendicular to the photon propagation direction and parallel to the electric polarization direction. For the measured data, the error in the XPS intensity is expected to be better than 1%. The error in photon energy calibration is better than 0.05 eV.

X-ray total scattering was performed at the 28-ID-2 beamline of the National Synchrotron Light Source II of Brookhaven National Laboratory, using a photon wavelength of 0.1819 Å. The raw data were integrated using Dioptas software[64], followed by intensity correction, background removal, and Fourier transform in PDFgetx3 to obtain the PDF data.[65]

Molecular Modeling: Reduction potentials are computed relative to Li^+/Li as the difference between free energies of solvates (A) and their reduced (A^-) states using eq. 1

$$E^{re/ox} = \frac{\Delta G(A \rightarrow A^-)}{F} - 1.4, \quad (1)$$

where F is Faraday's constant. The final figure of -1.4 V accounts for shifting the computed potential to the Li^+/Li scale.[66] An additional error of the order of 0.1–0.3 V is expected for the conversion factor from the absolute scale to Li^+/Li in nonaqueous solvents as previously discussed.[66] It is consistent with the previous report of the variation of the lithium free energy of solvation in water, methanol, acetonitrile, hydrazine, and ammonia.[67] Gaussian 16 C.02 package was used in conjunction of PCM(ε=20)/ ωB97XD/6-31+G(d,p) DFT [68, 69]. Our previous calculations for the esters containing a -CHF_2 group showed that low computational cost ωB97XD/6-31+G(d,p) DFT calculations predicted reduction potential within 0.32 V of the more reliable and computationally expensive composite G4MP2 calculations as discussed in Xu et al.[1] This level previously predicted reduction potentials of Li^+/DEC, Li^+/DMC, Li^+/EMC, Li^+/EC in the range of 0.5–0.68 V, which is in good agreement with previous experiments and G4MP4 calculations.[70]

MD simulations were performed on LP40 and FLC electrolytes with simulation boxes comprised of 64 $LiPF_6$ dissolved in 228 EC and 210 DEC and 96 LiFSI dissolved in 132 FEC and 286 DFDEC and a 342, respectively. Two replicas of FLC electrolytes were simulated. After initial equilibration at 363 K for 4 ns, each system was equilibrated at 333 K for 23 ns followed by production runs of 223–284 ns for FLC electrolyte and 330 ns for LP40. Simulations at 298 K were 520-550 ns after 22 ns equilibration for FLC electrolyte and 329 ns for LP40. To ensure equilibration of structural properties, it is important that the Li+ cations would exchange solvent and anions at least a few times. The calculated residence times[71] for the Li-Oc(FEC), Li-Oc(DFDEC) and Li-N(FSI) were 1.6 ns, 6.4 ns and 3.7 ns establishing the timescale for equilibration of the distribution of ionic aggregates and Li^+ solvates at room temperature. The equilibration runs were multiple times longer than the longest residence time between the Li^+ and anions, ensuring structural equilibration. A time reversible (RESPA) integrator utilized three-time steps: i) integrating the contribution from bonds and angles to the forces were calculated at any 0.5 fs, ii) the contribution of dihedrals and non-bonded forces within 7 Å cut-off was updated at any 1.5 fs, and iii) the remainder of the forces (reciprocal space Ewald using $k=8^3$ vectors) and non-bonded forces within 12 Å cut-off was updated at any 3 fs. Nose-Hoover thermostat was used for temperature control with the associated frequency of 0.01 fs^{-1}. The induced dipoles (μ) were found self-consistently at each 3 fs timestep with the tolerance of $\mu^2 < 10^{-12}$ $(e^*Å)^2$. A previously developed many-body polarizable APPLE&P force field [72-74] was used with the force field parameters given in the attached archive for FLC electrolyte.

Conductivity, viscosity and ion self-diffusion coefficients were extracted using a previously discussed methodology that included the application of the finite size correction to self-diffusion coefficients and conductivity.[72] A plateau

between 1 ns and 3 ns was used to extract t_+^{COM} and degree of ionic correlation motion a_d (ionicity) as shown in Figure S5. Conductivity (σ) is typically determined from MD simulations using Einstein relation

$$\sigma = \lim_{t\to\infty} \frac{e^2}{6tVk_BT} \sum_{i,j}^{N} z_i z_j \langle([\mathbf{R}_i(t) - \mathbf{R}_i(0)])([\mathbf{R}_j(t) - \mathbf{R}_j(0)])\rangle$$

$$\sigma = \sigma_+^{self} + \sigma_-^{self} + \sigma_{++}^{d} + \sigma_{--}^{d} - 2\sigma_{+-}$$

where e is the electron charge, V is the volume of the sample, k_B is Boltzmann's constant, T is the temperature and n_+ and n_- are the number of cations and anions, respectively. The full matrix of the charge displacement contributions to conductivity could be decomposed to the self-diffusion contributions coming from the diagonal terms $\sigma_+^{self} + \sigma_-^{self}$, the off-diagonal terms arising from the correlation of distinct cation – cations and anion – anion motion $\sigma_{++}^{d} + \sigma_{--}^{d}$ and the off-diagonal distinct anion – anion motion. Taking only the contributions due to positive ion motion from the full matrix of displacements $[\sigma_+^{self} + \sigma_{++}^{d} - \sigma_{+-}]/\sigma$ allows one to estimate transference number in the center of mass frame.[75]

In the case when all ions are dissociated, and their motion is uncorrelated the off-diagonal components could be neglected, i. e $\sigma_{++}^{d} + \sigma_{--}^{d} - 2\sigma_{+-} = 0$ and one recovers Nernst-Einstein equation for the uncorrelated conductivity κ_{uncorr}

$$\sigma_{uncorr} = \frac{e^2}{Vk_BT}(n_+D_+ + n_-D_-)$$

Thus, the ratio of conductivity to σ_{uncorr} characterizes the degree of ion uncorrelated motion that is also called ionicity or inverse Haven ratio

$$\alpha_d = H_R^{-1} = \frac{\sigma}{\sigma_{uncorr.}} = \frac{\sigma_+^{self} + \sigma_-^{self} + \sigma_{++}^{d} + \sigma_{--}^{d} - 2\sigma_{+-}}{\sigma^{self}}$$

Plotting $\alpha_d(t)$ as a function of simulation time and finding a plateau allows one to better assess error bars for $\alpha_d(t)$ as shown in Figure S5.

The difference between the solvent and ion self-diffusion coefficients extracted from two replicas of FLC electrolyte was below 1.5% indicating the magnitude of statistical uncertainty. The difference between the Li^+ coordination numbers extracted from replica 1 and 2 of FLC electrolyte was below 1%.

ASSOCIATED CONTENT

Supporting Information. Electrochemical results of various electrolytes, MD simulation snapshots, DFT calculated reduction potentials, morphology and structure of pristine and cycled electrodes, XPS spectra, ionic conductivity, electrochemical performance at high current densities, comparison of this work and other reported electrolytes. This material is available free of charge via the Internet at http://pubs.acs.org.

AUTHOR INFORMATION

Corresponding Author

* Email: enhu@bnl.gov (E.H.)

Notes

Authors declare that they have no competing interests.

Disclaimer

Certain commercial equipment, instruments, or materials are identified in this paper in order to specify the experimental procedure adequately, and do not represent an endorsement by the National Institute of Standards and Technology.

ACKNOWLEDGMENT

The work done at BNL is supported by the Assistant Secretary for Energy Efficiency and Renewable Energy (EERE), Vehicle Technology Office (VTO) of the US Department of Energy (DOE) through the Advanced Battery Materials Research (BMR) Program under contract no. DE-SC0012704. This research used 28-ID-2 (XPD) beamline, 7-ID-2 (SST-2) beamline (managed by National Institute of Standards and Technology) of the National Synchrotron Light Source II, US DOE Office of Science User Facilities operated for the DOE Office of Science by BNL under contract no. DE-SC0012704. SEM, XRD measurements used the resources of the Center for Functional Nanomaterials, a US DOE Office of Science User Facility at BNL, under contract no. DE-SC0012704. We also acknowledge the US DOE CAMP (Cell Analysis, Modeling and Prototyping) Facility, Argonne National Laboratory for supplying the graphite, NMC622, NMC811 electrodes. The CAMP Facility is fully supported by the DOE Vehicle Technologies Office. Part of the molecular modeling performed at ARL was supported by the Assistant Secretary for Energy Efficiency and Renewable Energy, Vehicle Technology Office of the U.S. DOE via interagency agreement 89243319SEE000004 and DEVCOM ARL. Part of the modeling work in this research used resources of the National Energy Research Scientific Computing Center (NERSC), a Department of Energy Office of Science User Facility using NERSC award ERCAP0028828.

REFERENCES

(1) Xu, J.; Zhang, J.; Pollard, T. P.; Li, Q.; Tan, S.; Hou, S.; Wan, H.; Chen, F.; He, H.; Hu, E.; et al. Electrolyte design for Li-ion batteries under extreme operating conditions. *Nature* **2023**, *614* (7949), 694-700.

(2) Peled, E.; Menkin, S. Review—SEI: Past, Present and Future. *J. Electrochem. Soc.* **2017**, *164* (7), A1703.

(3) Shadike, Z.; Tan, S.; Lin, R.; Cao, X.; Hu, E.; Yang, X.-Q. Engineering and characterization of interphases for lithium metal anodes. *Chem. Sci.* **2022**, *13* (6), 1547-1568.

(4) Yan, C.; Li, H.-R.; Chen, X.; Zhang, X.-Q.; Cheng, X.-B.; Xu, R.; Huang, J.-Q.; Zhang, Q. Regulating the Inner Helmholtz Plane for Stable Solid Electrolyte Interphase on Lithium Metal Anodes. *J. Am. Chem. Soc.* **2019**, *141* (23), 9422-9429.

(5) Wang, A.; Kadam, S.; Li, H.; Shi, S.; Qi, Y. Review on modeling of the anode solid electrolyte interphase (SEI) for lithium-ion batteries. *Npj Comput. Mater.* **2018**, *4* (1), 15.

(6) Perez Beltran, S.; Balbuena, P. B. SEI formation mechanisms and Li+ dissolution in lithium metal anodes: Impact of the electrolyte composition and the electrolyte-to-anode ratio. *J. Power Sources* **2022**, *551*, 232203.

(7) Tan, S.; Shadike, Z.; Li, J.; Wang, X.; Yang, Y.; Lin, R.; Cresce, A.; Hu, J.; Hunt, A.; Waluyo, I.; et al. Additive engineering for robust interphases to stabilize high-Ni layered structures at ultra-high voltage of 4.8 V. *Nat. Energy* **2022**, *7* (6), 484-494.

(8) Xu, J. Critical Review on cathode–electrolyte Interphase Toward High-Voltage Cathodes for Li-Ion Batteries. *Nanomicro Lett.* **2022**, *14* (1), 166.

(9) Hestenes, J. C.; Marbella, L. E. Beyond Composition: Surface Reactivity and Structural Arrangement of the Cathode–Electrolyte Interphase. *ACS Energy Lett.* **2023**, *8* (11), 4572-4596.
(10) Wu, Q.; McDowell, M. T.; Qi, Y. Effect of the Electric Double Layer (EDL) in Multicomponent Electrolyte Reduction and Solid Electrolyte Interphase (SEI) Formation in Lithium Batteries. *J. Am. Chem. Soc.* **2023**, *145* (4), 2473-2484.
(11) Hou, J.; Yang, M.; Wang, D.; Zhang, J. Fundamentals and Challenges of Lithium Ion Batteries at Temperatures between −40 and 60 °C. *Adv. Energy Mater.* **2020**, *10* (18), 1904152.
(12) Ringsby, A. J.; Fong, K. D.; Self, J.; Bergstrom, H. K.; McCloskey, B. D.; Persson, K. A. Transport Phenomena in Low Temperature Lithium-Ion Battery Electrolytes. *J. Electrochem. Soc.* **2021**, *168* (8), 080501.
(13) Xu, R.; Zhang, S.; Shen, X.; Yao, N.; Ding, J.-F.; Xiao, Y.; Xu, L.; Yan, C.; Huang, J.-Q. Unlocking the Polarization and Reversibility Limitations for Stable Low-Temperature Lithium Metal Anodes. *Small Structures* **2023**, *4* (7), 2200400.
(14) Zhang, S.; Ding, J.-F.; Xu, R.; Xiao, Y.; Yan, C.; Huang, J.-Q. Temperature-Mediated Dynamic Lithium Loss and its Implications for High-Efficiency Lithium Metal Anodes. *Adv. Energy Mater.* **2024**, *14* (9), 2303726.
(15) Horstmann, B.; Shi, J.; Amine, R.; Werres, M.; He, X.; Jia, H.; Hausen, F.; Cekic-Laskovic, I.; Wiemers-Meyer, S.; Lopez, J.; et al. Strategies towards enabling lithium metal in batteries: interphases and electrodes. *Energy Environ. Sci.* **2021**, *14* (10), 5289-5314.
(16) Jia, H.; Xu, Y.; Burton, S. D.; Gao, P.; Zhang, X.; Matthews, B. E.; Engelhard, M. H.; Zhong, L.; Bowden, M. E.; Xiao, B.; et al. Enabling Ether-Based Electrolytes for Long Cycle Life of Lithium-Ion Batteries at High Charge Voltage. *ACS Appl. Mater. Interfaces* **2020**, *12* (49), 54893-54903.
(17) Zhang, X.; Zou, L.; Xu, Y.; Cao, X.; Engelhard, M. H.; Matthews, B. E.; Zhong, L.; Wu, H.; Jia, H.; Ren, X.; et al. Advanced Electrolytes for Fast-Charging High-Voltage Lithium-Ion Batteries in Wide-Temperature Range. *Adv. Energy Mater.* **2020**, *10* (22), 2000368.
(18) Ren, X.; Zou, L.; Cao, X.; Engelhard, M. H.; Liu, W.; Burton, S. D.; Lee, H.; Niu, C.; Matthews, B. E.; Zhu, Z.; et al. Enabling High-Voltage Lithium-Metal Batteries under Practical Conditions. *Joule* **2019**, *3* (7), 1662-1676.
(19) Cao, X.; Gao, P.; Ren, X.; Zou, L.; Engelhard, M. H.; Matthews, B. E.; Hu, J.; Niu, C.; Liu, D.; Arey, B. W.; et al. Effects of fluorinated solvents on electrolyte solvation structures and electrode/electrolyte interphases for lithium metal batteries. *Proc. Natl. Acad. Sci. U.S. A.* **2021**, *118* (9), e2020357118.
(20) Ren, X.; Gao, P.; Zou, L.; Jiao, S.; Cao, X.; Zhang, X.; Jia, H.; Engelhard, M. H.; Matthews, B. E.; Wu, H.; et al. Role of inner solvation sheath within salt–solvent complexes in tailoring electrode/electrolyte interphases for lithium metal batteries. *Proc. Natl. Acad. Sci. U.S. A.* **2020**, *117* (46), 28603-28613.
(21) Yu, Z.; Rudnicki, P. E.; Zhang, Z.; Huang, Z.; Celik, H.; Oyakhire, S. T.; Chen, Y.; Kong, X.; Kim, S. C.; Xiao, X.; et al. Rational solvent molecule tuning for high-performance lithium metal battery electrolytes. *Nat. Energy* **2022**, *7* (1), 94-106.
(22) Yu, Z.; Wang, H.; Kong, X.; Huang, W.; Tsao, Y.; Mackanic, D. G.; Wang, K.; Wang, X.; Huang, W.; Choudhury, S.; et al. Molecular design for electrolyte solvents enabling energy-dense and long-cycling lithium metal batteries. *Nat. Energy* **2020**, *5* (7), 526-533.
(23) Chen, Y.; Yu, Z.; Rudnicki, P.; Gong, H.; Huang, Z.; Kim, S. C.; Lai, J.-C.; Kong, X.; Qin, J.; Cui, Y.; et al. Steric Effect Tuned Ion Solvation Enabling Stable Cycling of High-Voltage Lithium Metal Battery. *J. Am. Chem. Soc.* **2021**, *143* (44), 18703-18713.
(24) Chen, Y.; Yu, Z.; Gong, H.; Zhang, W.; Rudnicki, P. E.; Huang, Z.; Yu, W.; Kim, S. C.; Boyle, D. T.; Sayavong, P.; et al. Failure Process During Fast Charging of Lithium Metal Batteries with Weakly Solvating Fluoroether Electrolytes. *J. Phys. Chem. C* **2024**, *128* (28), 11487-11497.
(25) Yoo, D.-J.; Liu, Q.; Cohen, O.; Kim, M.; Persson, K. A.; Zhang, Z. Understanding the Role of SEI Layer in Low-Temperature Performance of Lithium-Ion Batteries. *ACS Appl. Mater. Interfaces* **2022**, *14* (9), 11910-11918.
(26) Xia, J.; Glazier, S. L.; Petibon, R.; Dahn, J. R. Improving Linear Alkyl Carbonate Electrolytes with Electrolyte Additives. *J. Electrochem. Soc.* **2017**, *164* (6), A1239-A1250.
(27) Nan, B.; Chen, L.; Rodrigo, N. D.; Borodin, O.; Piao, N.; Xia, J.; Pollard, T.; Hou, S.; Zhang, J.; Ji, X.; et al. Enhancing Li(+) Transport in NMC811||Graphite Lithium-Ion Batteries at Low Temperatures by Using Low-Polarity-Solvent Electrolytes. *Angew. Chem. Int. Ed.* **2022**, *61* (35), e202205967.
(28) Wang, J.; Yamada, Y.; Sodeyama, K.; Chiang, C. H.; Tateyama, Y.; Yamada, A. Superconcentrated electrolytes for a high-voltage lithium-ion battery. *Nat. Commun.* **2016**, *7* (1), 12032.
(29) Kang, G.; Zhong, G.; Ma, J.; Yin, R.; Cai, K.; Jia, T.; Ren, X.; Yu, K.; Qin, P.; Chen, Z.; et al. Weakly solvated EC-free linear alkyl carbonate electrolytes for Ni-rich cathode in rechargeable lithium battery. *iScience* **2022**, *25* (12), 105710.
(30) Ko, S.; Han, X.; Shimada, T.; Takenaka, N.; Yamada, Y.; Yamada, A. Electrolyte design for lithium-ion batteries with a cobalt-free cathode and silicon oxide anode. *Nat. Sustain.* **2023**, *6* (12), 1705-1714.
(31) Lee, H.; An, H.; Chang, H.; Lee, M.; Park, S.; Lee, S.; Kang, J.; Byon, S.; Koo, B.; Lee, H.; et al. Boosting interfacial kinetics in extremely fast rechargeable Li-ion batteries with linear carbonate-based, LiPF6-concentrated electrolyte. *Energy Storage Mater.* **2023**, *63*, 102995.
(32) Yu, Z.; Yu, W.; Chen, Y.; Mondonico, L.; Xiao, X.; Zheng, Y.; Liu, F.; Hung, S. T.; Cui, Y.; Bao, Z. Tuning Fluorination of Linear Carbonate for Lithium-Ion Batteries. *J. Electrochem. Soc.* **2022**, *169* (4), 040555.
(33) Lu, D.; Li, R.; Rahman, M. M.; Yu, P.; Lv, L.; Yang, S.; Huang, Y.; Sun, C.; Zhang, S.; Zhang, H.; et al. Ligand-channel-enabled ultrafast Li-ion conduction. *Nature* **2024**, *627* (8002), 101-107.
(34) Mo, Y.; Liu, G.; Yin, Y.; Tao, M.; Chen, J.; Peng, Y.; Wang, Y.; Yang, Y.; Wang, C.; Dong, X.; et al. Fluorinated Solvent Molecule Tuning Enables Fast-Charging and Low-Temperature Lithium-Ion Batteries. *Adv. Energy Mater.* **2023**, *13* (32), 2301285.
(35) Xu, K. Nonaqueous Liquid Electrolytes for Lithium-Based Rechargeable Batteries. *Chem. Rev.* **2004**, *104* (10), 4303-4418.
(36) Chen, Y.; He, Q.; Zhao, Y.; Zhou, W.; Xiao, P.; Gao, P.; Tavajohi, N.; Tu, J.; Li, B.; He, X.; et al. Breaking solvation dominance of ethylene carbonate via molecular charge engineering enables lower temperature battery. *Nat. Commun.* **2023**, *14* (1), 8326.
(37) Lin, Y.; Yu, Z.; Yu, W.; Liao, S.-L.; Zhang, E.; Guo, X.; Huang, Z.; Chen, Y.; Qin, J.; Cui, Y.; et al. Impact of the fluorination degree of ether-based electrolyte solvents on Li-metal battery performance. *J. Mater. Chem. A* **2024**, *12* (5), 2986-2993.
(38) Yin, Y.; Yang, Y.; Cheng, D.; Mayer, M.; Holoubek, J.; Li, W.; Raghavendran, G.; Liu, A.; Lu, B.; Davies, D. M.; et al. Fire-extinguishing, recyclable liquefied gas electrolytes for temperature-resilient lithium-metal batteries. *Nat. Energy* **2022**, *7* (6), 548-559.
(39) Han, H.-B.; Zhou, S.-S.; Zhang, D.-J.; Feng, S.-W.; Li, L.-F.; Liu, K.; Feng, W.-F.; Nie, J.; Li, H.; Huang, X.-J.; et al. Lithium bis(fluorosulfonyl)imide (LiFSI) as conducting salt for nonaqueous liquid electrolytes for lithium-ion batteries: Physicochemical and electrochemical properties. *J. Power Sources* **2011**, *196* (7), 3623-3632.
(40) Nie, M.; Demeaux, J.; Young, B. T.; Heskett, D. R.; Chen, Y.; Bose, A.; Woicik, J. C.; Lucht, B. L. Effect of Vinylene Carbonate and Fluoroethylene Carbonate on SEI Formation on Graphitic Anodes in Li-Ion Batteries. *J. Electrochem. Soc.* **2015**, *162* (13), A7008.
(41) Borodin, O.; Olguin, M.; Spear, C. E.; Leiter, K. W.; Knap, J. Towards high throughput screening of electrochemical stability of battery electrolytes. *Nanotechnology* **2015**, *26* (35), 354003.
(42) Yao, N.; Chen, X.; Fu, Z.-H.; Zhang, Q. Applying Classical, Ab Initio, and Machine-Learning Molecular Dynamics Simulations to the Liquid Electrolyte for Rechargeable Batteries. *Chem. Rev.* **2022**, *122* (12), 10970-11021.

(43) Hayamizu, K. Temperature Dependence of Self-Diffusion Coefficients of Ions and Solvents in Ethylene Carbonate, Propylene Carbonate, and Diethyl Carbonate Single Solutions and Ethylene Carbonate + Diethyl Carbonate Binary Solutions of LiPF6 Studied by NMR. *J. Chem. Eng. Data* **2012**, *57* (7), 2012-2017.
(44) Ma, B.; Zhang, H.; Li, R.; Zhang, S.; Chen, L.; Zhou, T.; Wang, J.; Zhang, R.; Ding, S.; Xiao, X.; et al. Molecular-docking electrolytes enable high-voltage lithium battery chemistries. *Nat. Chem.* **2024**, *16* (9), 1427-1435.
(45) Smith, A. J.; Burns, J. C.; Trussler, S.; Dahn, J. R. Precision Measurements of the Coulombic Efficiency of Lithium-Ion Batteries and of Electrode Materials for Lithium-Ion Batteries. *J. Electrochem. Soc.* **2010**, *157* (2), A196.
(46) Hou, T.; Yang, G.; Rajput, N. N.; Self, J.; Park, S.-W.; Nanda, J.; Persson, K. A. The influence of FEC on the solvation structure and reduction reaction of LiPF6/EC electrolytes and its implication for solid electrolyte interphase formation. *Nano Energy* **2019**, *64*, 103881.
(47) Spotte-Smith, E. W. C.; Petrocelli, T. B.; Patel, H. D.; Blau, S. M.; Persson, K. A. Elementary Decomposition Mechanisms of Lithium Hexafluorophosphate in Battery Electrolytes and Interphases. *ACS Energy Lett.* **2023**, *8* (1), 347-355.
(48) Li, Z.; Wang, L.; Huang, X.; He, X. Unveiling the Mystery of LiF within Solid Electrolyte Interphase in Lithium Batteries. *Small* **2024**, *20* (22), 2305429.
(49) Zhao, J.; Liao, L.; Shi, F.; Lei, T.; Chen, G.; Pei, A.; Sun, J.; Yan, K.; Zhou, G.; Xie, J.; et al. Surface Fluorination of Reactive Battery Anode Materials for Enhanced Stability. *J. Am. Chem. Soc.* **2017**, *139* (33), 11550-11558.
(50) Liu, S.; Ji, X.; Yue, J.; Hou, S.; Wang, P.; Cui, C.; Chen, J.; Shao, B.; Li, J.; Han, F.; et al. High Interfacial-Energy Interphase Promoting Safe Lithium Metal Batteries. *J. Am. Chem. Soc.* **2020**, *142* (5), 2438-2447.
(51) Yang, G.; Frisco, S.; Tao, R.; Philip, N.; Bennett, T. H.; Stetson, C.; Zhang, J.-G.; Han, S.-D.; Teeter, G.; Harvey, S. P.; et al. Robust Solid/Electrolyte Interphase (SEI) Formation on Si Anodes Using Glyme-Based Electrolytes. *ACS Energy Lett.* **2021**, *6* (5), 1684-1693.
(52) Qiao, L.; Oteo, U.; Martinez-Ibañez, M.; Santiago, A.; Cid, R.; Sanchez-Diez, E.; Lobato, E.; Meabe, L.; Armand, M.; Zhang, H. Stable non-corrosive sulfonimide salt for 4-V-class lithium metal batteries. *Nat. Mater.* **2022**, *21* (4), 455-462.
(53) Jiao, S.; Ren, X.; Cao, R.; Engelhard, M. H.; Liu, Y.; Hu, D.; Mei, D.; Zheng, J.; Zhao, W.; Li, Q.; et al. Stable cycling of high-voltage lithium metal batteries in ether electrolytes. *Nat. Energy* **2018**, *3* (9), 739-746.
(54) Kamphaus, E. P.; Gomez, S. A.; Qin, X.; Shao, M.; Balbuena, P. B. Effects of Solid Electrolyte Interphase Components on the Reduction of LiFSI over Lithium Metal. *ChemPhysChem* **2020**, *21* (12), 1310-1317.
(55) Fan, X.; Ji, X.; Chen, L.; Chen, J.; Deng, T.; Han, F.; Yue, J.; Piao, N.; Wang, R.; Zhou, X.; et al. All-temperature batteries enabled by fluorinated electrolytes with non-polar solvents. *Nat. Energy* **2019**, *4* (10), 882-890.
(56) Alvarado, J.; Schroeder, M. A.; Pollard, T. P.; Wang, X.; Lee, J. Z.; Zhang, M.; Wynn, T.; Ding, M.; Borodin, O.; Meng, Y. S.; et al. Bisalt ether electrolytes: a pathway towards lithium metal batteries with Ni-rich cathodes. *Energy Environ. Sci.* **2019**, *12* (2), 780-794.
(57) Fang, M.; Du, B.; Zhang, X.; Dong, X.; Yue, X.; Liang, Z. An Electrolyte with Less Space-Occupying Diluent at Cathode Inner Helmholtz Plane for Stable 4.6 V Lithium-Ion Batteries. *Angew. Chem. Int. Ed.* **2024**, *63* (3), e202316839.
(58) Zou, Y.; Ma, Z.; Liu, G.; Li, Q.; Yin, D.; Shi, X.; Cao, Z.; Tian, Z.; Kim, H.; Guo, Y.; et al. Non-Flammable Electrolyte Enables High-Voltage and Wide-Temperature Lithium-Ion Batteries with Fast Charging. *Angew. Chem. Int. Ed.* **2023**, *62* (8), e202216189.
(59) Qin, M.; Liu, M.; Zeng, Z.; Wu, Q.; Wu, Y.; Zhang, H.; Lei, S.; Cheng, S.; Xie, J. Rejuvenating Propylene Carbonate-based Electrolyte Through Nonsolvating Interactions for Wide-Temperature Li-ions Batteries. *Adv. Energy Mater.* **2022**, *12* (48), 2201801.
(60) Liu, B.; Li, Q.; Engelhard, M. H.; He, Y.; Zhang, X.; Mei, D.; Wang, C.; Zhang, J.-G.; Xu, W. Constructing Robust Electrode/Electrolyte Interphases to Enable Wide Temperature Applications of Lithium-Ion Batteries. *ACS Appl. Mater. Interfaces* **2019**, *11* (24), 21496-21505.
(61) Wang, J.; Zheng, Q.; Fang, M.; Ko, S.; Yamada, Y.; Yamada, A. Concentrated Electrolytes Widen the Operating Temperature Range of Lithium-Ion Batteries. *Adv. Sci.* **2021**, *8* (18), 2101646.
(62) Luo, L.; Chen, K.; Chen, H.; Li, H.; Cao, R.; Feng, X.; Chen, W.; Fang, Y.; Cao, Y. Enabling Ultralow-Temperature (−70 °C) Lithium-Ion Batteries: Advanced Electrolytes Utilizing Weak-Solvation and Low-Viscosity Nitrile Cosolvent. *Adv. Mater.* **2024**, *36* (5), 2308881.
(63) Zhao, Y.; Hu, Z.; Zhao, Z.; Chen, X.; Zhang, S.; Gao, J.; Luo, J. Strong Solvent and Dual Lithium Salts Enable Fast-Charging Lithium-Ion Batteries Operating from −78 to 60 °C. *J. Am. Chem. Soc.* **2023**, *145* (40), 22184-22193.
(64) Prescher, C.; Prakapenka, V. B. DIOPTAS: a program for reduction of two-dimensional X-ray diffraction data and data exploration. *High Press. Res.* **2015**, *35* (3), 223-230.
(65) Juhas, P.; Davis, T.; Farrow, C. L.; Billinge, S. J. L. PDFgetX3: a rapid and highly automatable program for processing powder diffraction data into total scattering pair distribution functions. *J. Appl. Cryst.* **2013**, *46* (2), 560-566.
(66) Borodin, O.; Behl, W.; Jow, T. R. Oxidative Stability and Initial Decomposition Reactions of Carbonate, Sulfone, and Alkyl Phosphate-Based Electrolytes. *J. Phys. Chem. C* **2013**, *117* (17), 8661-8682.
(67) Gomer, R.; Tryson, G. An experimental determination of absolute half-cell emf's and single ion free energies of solvation. *J. Chem. Phys.* **1977**, *66* (10), 4413-4424.
(68) *Gaussian 16 Rev. C.01*; Wallingford, CT, 2016. (accessed.
(69) Chai, J.-D.; Head-Gordon, M. Long-range corrected hybrid density functionals with damped atom–atom dispersion corrections. *Phys. Chem. Chem. Phys.* **2008**, *10* (44), 6615-6620.
(70) Delp, S. A.; Borodin, O.; Olguin, M.; Eisner, C. G.; Allen, J. L.; Jow, T. R. Importance of Reduction and Oxidation Stability of High Voltage Electrolytes and Additives. *Electrochim. Acta* **2016**, *209*, 498-510.
(71) Borodin, O.; Smith, G. D. Quantum Chemistry and Molecular Dynamics Simulation Study of Dimethyl Carbonate: Ethylene Carbonate Electrolytes Doped with LiPF6. *J. Phys. Chem. B* **2009**, *113* (6), 1763-1776.
(72) Borodin, O. Polarizable Force Field Development and Molecular Dynamics Simulations of Ionic Liquids. *J. Phys. Chem. B* **2009**, *113* (33), 11463-11478.
(73) Han, S.-D.; Borodin, O.; Seo, D. M.; Zhou, Z.-B.; Henderson, W. A. Electrolyte Solvation and Ionic Association: V. Acetonitrile-Lithium Bis(fluorosulfonyl)imide (LiFSI) Mixtures. *J. Electrochem. Soc.* **2014**, *161* (14), A2042.
(74) Andersson, R.; Borodin, O.; Johansson, P. Dynamic Structure Discovery Applied to the Ion Transport in the Ubiquitous Lithium-ion Battery Electrolyte LP30. *J. Electrochem. Soc.* **2022**, *169* (10), 100540.
(75) Fang, C.; Mistry, A.; Srinivasan, V.; Balsara, N. P.; Wang, R. Elucidating the Molecular Origins of the Transference Number in Battery Electrolytes Using Computer Simulations. *JACS Au* **2023**, *3* (2), 306-315.

Table of Contents